Polarization Selective Optical Nonlinearities in Cold Rydberg Atoms

Jin-Hui Wu,[1] M. Artoni,[2,3] and G. C. La Rocca.[4]

[1]*Center for Quantum Sciences, Northeast Normal University, Changchun 130117, China.*
[2]*European Laboratory for Nonlinear Spectroscopy (LENS), 50019 Firenze, Italy.*
[3]*Department of Engineering and Information Technology & INO-CNR, Brescia University, 25133 Brescia, Italy.*
[4]*Scuola Normale Superiore and CNISM, 56126 Pisa, Italy.*

(Dated: October 10, 2015)

We study the interaction between a probe and a trigger *weak* field in an elongated dense sample of ultracold rubidium Rydberg atoms in the presence of a coupling and a dressing *strong* field. Dipole Rydberg blockade may occur and can be set to depend on the probe and trigger polarizations giving rise to diverse regimes of electromagnetically induced transparency (EIT) with a concomitant small probe and trigger absorption and dispersion. This is shown to be relevant to the implementation of polarization conditional probe and trigger cross-nonlinearities in cold Rydberg atoms.

PACS numbers: 42.50.Gy, 03.67.Lx, 32.80.Ee, 42.65.-k

I. INTRODUCTION

Photon-photon interactions enabled by nonlinear optical mechanisms play an important role in quantum information processing. Photons, in fact, are ideal carriers of quantum information as they can propagate at the speed of light and are generally not affected by the environment [1]. Large cross-phase non-linearities between two photons, in particular, are crucial in many quantum information applications. One of the preferred and widely explored scheme to enhance cross-phase nonlinearities is based on Kerr-EIT interactions between a probe field and a trigger pulse [2–5]. A major drawbacks, in this case, is the mismatch of the group velocities which limits the probe and signal interaction time, placing an upper limit on the order of a small fraction of a radian to the resulting cross-phase shift [6]. Large intensities are required instead to reach appreciable nonlinear modulations using Kerr-EIT like interactions [7]. To overcome this limit, matched double slow-light pulses with two atomic species [8] have been proposed as well as various other variant schemes including tripod [9–11], N-tripod [12, 13], and M-type [14, 15] level configurations and a tripod double EIT [3] and double slow light pulses in cold atoms [4].

Ultracold Rydberg atoms, on the other hand, are now attracting great attention [16, 17]. The unique combination of their strong dipole-dipole interactions and long radiative lifetimes can in fact be exploited to realize robust light-atom quantum interfaces [18–20] for quantum information processing purposes. Rydberg atoms may exhibit, in particular, a special cooperative nonlinearity [21] known as *Rydberg blockade* whereby the presence of an atom excited to a Rydberg level will shift out of resonance the corresponding Rydberg level of all nearby atoms prohibiting the simultaneous Rydberg excitation of two or more atoms within a given volume (corresponding to a so-called superatom) determined by their dipole-dipole interaction. Photons nonlinear interactions in the presence of a Rydberg blockade have been shown to occur in samples of cold Rydberg atoms when driven into a regime of EIT [22, 23]. This has been restrained, however, to considerations of absorptive and dispersive photon-photon interactions of a *single* light field. Extensions to conditional nonlinear interactions between *two* light fields are usually not straightforward [24–27].

The paper's main motivation is the discussion of a scheme for achieving large *conditional* nonlinear interactions between two *weak* optical fields with a concomitant small absorption and dispersion. We show that such conditional interactions can be achieved in samples of cold atoms through the polarization selective excitation of a high-lying Rydberg state the two weak fields couple to through different regimes of electromagnetically induced transparency. Specifically this is implemented under *symmetric*-EIT driving either through the inverted-Ψ (P) configuration of Fig.1(A) or through the two inverted-Y (Y) configurations of Fig. 1(B, C). *First*, this extends typical cooperative nonlinearities observed in Rydberg atoms, whose nonlinear response depends on the incident field intensity at a fixed polarization [28–30], to polarization-conditional cooperative nonlinearities. *Second*, different cooperative nonlinearities arising from specific probe and trigger polarization choices, through the selection of specific Rydberg excitation paths, give rise to different optical cross-nonlinearities between probe and trigger. Polarization-conditional interactions between these two weak fields enable us to devise polarization-encoded cross-nonlinearities exhibiting a large cross-phase modulation effect with little losses. *Third*, our polarization-conditional scheme takes place within the *same* ^{87}Rb superatom, at variance with what occurs, e.g., in cross-Kerr like [31], resonant absorbing [32], transversely separated [33], and site addressable [34] Rydberg nonlinearities. *Last* and at variance with a simple Kerr-gate that depends on the intensity of a control field [18-21] (scalar gate), our polarization selective optical nonlinearities scheme may be relevant to a Rydberg polarization-gate. The latter is a vector gate, with two or more independent photon states simultaneously present,

able to perform vector-state manipulations needed for quantum information processing.

We describe the evolution of the atoms internal variables through a standard set of Liouville eq.s briefly illustrated in the basic model of sect.II while the atomic response to the probe and trigger fields in the inverted-Ψ and in the two inverted-Y configurations are discussed respectively in sect. III(A) and sect. III(B, C).

The Rydberg blockade effect is discussed here by treating the atoms through a superatom (SA) model suitably including two-photon correlation [30, 35]. A detailed account of the Rydberg populations resulting from the three different polarization-dependent excitation paths of Fig. 1 is given in sect. IV(A) and IV(B).

Depending on whether or not the high Rydberg state is excited (*dipole blockade*) and depending on the polarization-excitation path selected, different cooperative Rydberg nonlinearities are observed. These will give rise in turn to different cooperative dispersion and absorption effects, which we study in sect. V for a pair of *monochromatic* probe and trigger fields under the different polarization configurations of Fig. 1. Concluding remarks about the paper's main results and their implications for polarization-encoded phase-gate applications are given in sect. VI.

II. THE BASIC MODEL.

Our aim is to exploit the Rydberg blockade to devise a *polarization selective* scheme leading to large cross-nonlinearities between two weak optical fields, say a probe and a trigger, yet minimising losses. We further seek a driving configuration that is *symmetric* as possible with respect to the probe and trigger transitions so as to avoid any group velocity mismatch between them as they simultaneously propagate through the sample.

A symmetric *inverted-Y* configuration of levels [Fig. 1(B,C)] would actually allow to couple probe and trigger, respectively, to the transitions from two distinct ground states to a common intermediate excited state which is, in turn, coupled to a higher Rydberg level via a strong dressing field in a ladder-like EIT level scheme. The distinct selection rules of the two lower transitions provide the required dependence on probe and trigger polarizations. However, when Rydberg blockade is turned on detuning the Rydberg level out of resonance, this inverted-Y configuration would become a highly absorbing one. Yet, by adding a strong coupling field resonant with the transition from a third ground state to the intermediate excited state, so as to realize a symmetric *inverted*-Ψ configuration of levels [Fig. 1(A)], we can prevent absorption. Even when the Rydberg level is shifted out of resonance making the presence of the dressing field immaterial, this coupling field allows for a nearly lossless propagation of probe and trigger in a lambda-like EIT configuration of levels.

Probe and trigger will then exhibit in general different absorption and dispersion properties depending on their polarizations. The inverted-Ψ configuration, in particular, appears to be a natural choice to achieve the above tasks of polarization selectivity and symmetric driving accompanied by small losses. This scheme, where probe and trigger are treated on equal footing, may also be relevant to cross-phase modulation applications.

A. Symmetric inverted-Ψ configuration.

We specifically consider an elongated sample of N cold ^{87}Rb atoms located at fixed positions and illuminated by two strong laser fields of amplitudes $\mathbf{E}_c$ and $\mathbf{E}_d$ and two weak laser fields of amplitudes $\mathbf{E}_p$ and $\mathbf{E}_t$. The coupling (ω_c) and dressing (ω_d) fields are assumed to have fixed *linear* polarizations while the probe (ω_p) and trigger (ω_t) fields may change from *left* to *right* circular polarizations or vice versa [Fig. 1(A-C)] and all four fields with respective frequencies ω_p, ω_t, ω_c, and ω_d interact with the five levels $|g\rangle$, $|m\rangle$, $|a\rangle$, $|e\rangle$, and $|r\rangle$.

The inverted-Ψ configuration (case $A1$), with dipole-allowed transitions $|g\rangle \leftrightarrow |e\rangle$, $|m\rangle \leftrightarrow |e\rangle$, $|a\rangle \leftrightarrow |e\rangle$, and $|e\rangle \leftrightarrow |r\rangle$, is attained with the "right" [↞ or rather "allowed" ?] choice of probe and trigger circular polarizations, namely a right-circular polarized probe (σ_p^+) and a left-circular polarized trigger (σ_t^-). We further assume that (i) only levels $|g\rangle$ and $|m\rangle$ are initially populated and (ii) both probe and trigger fields are so weak that levels $|a\rangle$, $|e\rangle$, and $|r\rangle$ are approximately empty. The resulting frequency detunings (Rabi frequencies) are defined as $\delta_p = \omega_p - \omega_{eg}$ ($\Omega_p = \mathbf{E}_p\mathbf{d}_{ge}/2\hbar$), $\delta_t = \omega_t - \omega_{em}$ ($\Omega_t = \mathbf{E}_t\mathbf{d}_{me}/2\hbar$), $\delta_c = \omega_c - \omega_{ea}$ ($\Omega_c = \mathbf{E}_c\mathbf{d}_{ae}/2\hbar$) and $\delta_d = \omega_d - \omega_{re}$ ($\Omega_d = \mathbf{E}_d\mathbf{d}_{er}/2\hbar$) with ω_{ij} being the resonant transition frequencies while $\mathbf{d}_{ij}$ being the electric dipole moments.

Adopting the *rotating-wave* and *electric-dipole* approximations, we first write down the interaction Hamiltonian for N cold atoms in the symmetric inverted-Ψ (P) configuration as

$$H_I = -\hbar\sum_{k=1}^{N}\left[\delta_p\sigma_{ee}^{Pk} + \Delta_m\sigma_{mm}^{Pk} + \Delta_a\sigma_{aa}^{Pk} + \Delta_r\sigma_{rr}^{Pk}\right] - \hbar\sum_{k=1}^{N}\left[\Omega_p\sigma_{eg}^{Pk} + \Omega_t\sigma_{em}^{Pk} + \Omega_c\sigma_{ea}^{Pk} + \Omega_d\sigma_{re}^{Pk} + h.c.\right] \quad (1)$$

with $\Delta_m = (\delta_p - \delta_t)$, $\Delta_a = (\delta_p - \delta_c)$, and $\Delta_r = (\delta_p + \delta_d)$ defined as two-photon detunings. After a standard

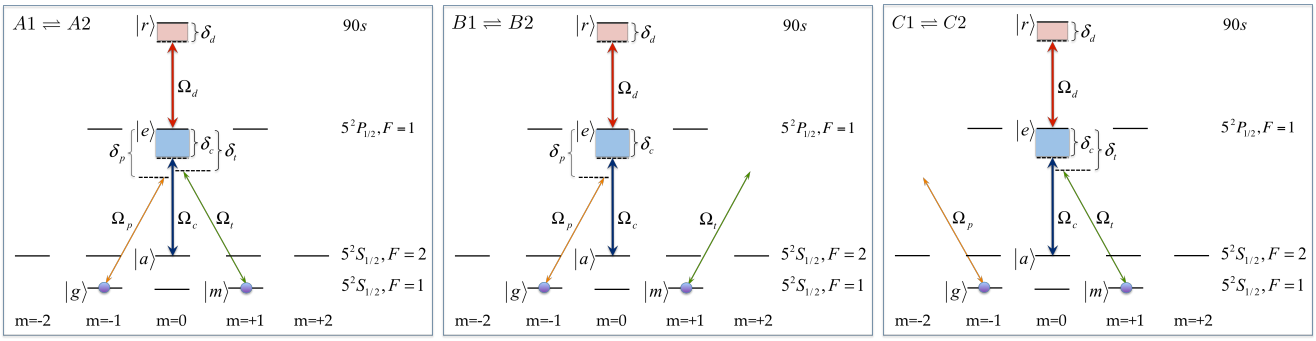

FIG. 1: (*Color online*) Level diagrams of cold ^{87}Rb atoms driven into the inverted-Ψ (*A1*) and the inverted-Y (*B1,C1*) configurations. All atoms are equally distributed between the two ground levels $|g\rangle$ and $|m\rangle$ and transitions to the excited level $|e\rangle$ are induced by *weak* probe ω_p (*A,B*) and trigger ω_t (*A,C*) fields, respectively. The excited level $|e\rangle$ is further connected to ground level $|a\rangle$ and Rydberg level $|r\rangle$ by *strong* coupling (ω_c) and dressing (ω_d) fields, respectively. The excitation of level $|r\rangle$ depends on the specific (circular) polarizations of probe and trigger and so is the Rydberg blockade effect (*see text*). Atoms inside a superatom (SA) containing one Rydberg excitation are driven into the tripod (*A2*) or lambda (*B2,C2*) configuration since strong dipole-dipole interactions now move $|r\rangle$ far off resonance. Such polarization selective dipole-dipole interactions give rise to two correlated regimes of electromagnetically induced transparency, namely, "inverted-Ψ ⇌ tripod" (*A1* ⇌ *A2*) and "inverted-Y ⇌ lambda" (*B1* ⇌ *B2* and *C1* ⇌ *C2*).

averaging of local atomic operators

$$\frac{1}{\delta n}\times\sum_{k=1}^{\delta n}\sigma_{ij}^{Pk}\rightarrow\sigma_{ij}^{P}(z) \tag{2}$$

in a micro volume δV containing δn atoms centered at z, we obtain the following Liouville equations

$$\begin{aligned}
\partial_t\sigma_{ge}^P &= -\gamma'_{ge}\sigma_{ge}^P + i\Omega_d^*\sigma_{gr}^P + i\Omega_c\sigma_{ga}^P + i\Omega_t\sigma_{gm}^P + i\Omega_p\sigma_{gg}^P\\
\partial_t\sigma_{ga}^P &= -\gamma'_{ga}\sigma_{ga}^P + i\Omega_c^*\sigma_{ge}^P\\
\partial_t\sigma_{gr}^P &= -\gamma'_{gr}\sigma_{gr}^P + i\Omega_d\sigma_{ge}^P\\
\partial_t\sigma_{me}^P &= -\gamma'_{me}\sigma_{me}^P + i\Omega_d^*\sigma_{mr}^P + i\Omega_c\sigma_{ma}^P + i\Omega_p\sigma_{mg}^P + i\Omega_t\sigma_{mm}^P\\
\partial_t\sigma_{ma}^P &= -\gamma'_{ma}\sigma_{ma}^P + i\Omega_c^*\sigma_{me}^P\\
\partial_t\sigma_{mr}^P &= -\gamma'_{mr}\sigma_{mr}^P + i\Omega_d\sigma_{me}^P\\
\partial_t\sigma_{gm}^P &= -\gamma'_{gm}\sigma_{gm}^P + i\Omega_t^\dagger\sigma_{ge}^P - i\Omega_p\sigma_{em}^P.
\end{aligned} \tag{3}$$

The remaining coherences and populations σ_{ea}^P, σ_{er}^P, σ_{ar}^P, σ_{ee}^P, σ_{aa}^P, and σ_{rr}^P are negligible in the limit of weak probe and trigger fields. We have phenomenologically introduced the complex dephasing rates $\gamma'_{ge}=\gamma_{ge}-i\delta_p$, $\gamma'_{ga}=\gamma_{ga}-i\Delta_a$, $\gamma'_{gr}=\gamma_{gr}-i\Delta_r$, $\gamma'_{gm}=\gamma_{gm}-i\Delta_m$, $\gamma'_{me}=\gamma_{me}-i\delta_t$, $\gamma'_{ma}=\gamma_{ma}-i\Delta'_a$ and $\gamma'_{mr}=\gamma_{mr}-i\Delta'_r$ in terms of the real dephasing rates γ_{ge}, γ_{ga}, γ_{gr}, γ_{gm}, γ_{me}, γ_{ma}, and γ_{mr} and two-photon detunings $\Delta'_a=\delta_t-\delta_c$ and $\Delta'_r=\delta_t+\delta_d$.

Note that the inverted–Ψ configuration, associated with the choice of the "right" [↫ or rather "allowed" ?] circular polarizations and no Rydberg blockade, i.e., the case (*A1*) in Fig. 1, is described by fully symmetric equations. By switching one or the other of the two circular polarizations, the full Ψ-configuration reduces to the asymmetric inverted-*Y* scheme (*B1*) or (*C1*) of Fig. 1. By switching both probe and trigger circular polarizations we end up to to a trivially symmetric and vacuum-like situation being both probe and trigger decoupled. On the other hand, when the Rydberg blockade is turned on and the level $|r\rangle$ is pushed out of resonance the full inverted–Ψ configuration (*A1*) of Fig. 1 reduces to the symmetric *tripod* configuration (*A2*) while the inverted-*Y* configuration (*B1*) reduces to the *lambda* configuration (*B2*) and so is for the reduction (*C1*) → (*C2*).

B. Reduced configurations.

The polarization selectivity stems from the selection rules of the $|g\rangle \leftrightarrow |e\rangle$ and $|m\rangle \leftrightarrow |e\rangle$ transitions. In particular, in the configuration $(B1)$ of Fig. 1 the trigger is decoupled from the $|m\rangle \leftrightarrow |e\rangle$ transition due to the "wrong" [↫ or rather "forbidden" ?] circular polarization (σ_t^+) which results into an inverted-Y configuration encompassing levels $|g\rangle$, $|a\rangle$, $|e\rangle$, and $|r\rangle$. Similarly, in the other inverted-Y configuration with levels $|m\rangle$, $|a\rangle$, $|e\rangle$, and $|r\rangle$ $(C1)$ the probe field is decoupled from the $|g\rangle \leftrightarrow |e\rangle$ transition due to a "wrong" [↫ or rather "forbidden" ?] circular polarization (σ_p^-). It is easy to attain the Liouville equations for the off-diagonal elements σ_{ij}^Y of these inverted-Y configuration ($B1$ or $C1$) by setting respectively $\Omega_t = 0$ or $\Omega_p = 0$ in Eqs. (3).

We further stress, in a mean-field sense, that one atom excited to a Rydberg level $|r\rangle$ shifts the same Rydberg level of all surrounding atoms due to strong dipole-dipole interactions (*Rydberg blockade*). Precisely, the excitation to $|r\rangle$ of atoms within a blockade sphere of radius R_b around the Rydberg excited atom is then strictly forbidden owing to a very large resonance shift. Consequently, within a mesoscopic blockade sphere, the probe (trigger) optical response is no longer described by the inverted-Ψ $(A1)$ or inverted-Y $(B1, C1)$ EIT configurations but rather by the basic tripod $(A2)$ or lambda $(B2, C2)$ EIT configurations (see Fig. 1). Relevant Liouville equations for off-diagonal elements σ_{ij}^T and σ_{ij}^L in the tripod and lambda configurations can be easily attained by further setting $\Omega_d = 0$ in the equations for σ_{ij}^P and σ_{ij}^Y of the inverted-Ψ and in the equations for the inverted-Y configuration, respectively. A detailed discussion of how such polarization selective dipole-dipole interactions give rise to cooperative nonlinearities in correlated EIT regimes – inverted-$\Psi \rightleftharpoons$ tripod ($A1 \rightleftharpoons A2$) and inverted-Y $\rightleftharpoons$ lambda ($B1 \rightleftharpoons B2$ and $C1 \rightleftharpoons C2$) – depending on the SA Rydberg populations will be provided in Sect. V.

III. ATOMIC SUSCEPTIBILITIES

We discuss in this section the probe and trigger steady-state susceptibilities for all six configurations of atomic levels examined in Fig. 1. These can be obtained from Eq.s (3) via a straightforward, albeit lengthy, calculation of relevant steady-state probe (σ_{ge}) and trigger (σ_{me}) atomic coherences, starting from the inverted-Ψ (P) configuration ($A1$).

A. Polarizations $\{\sigma_p^+, \sigma_t^-\}$.

For this choice of probe and trigger polarizations and for intensities such that $|\Omega_p|^2\sigma_{gg} = |\Omega_t|^2\sigma_{mm}$, the probe and trigger susceptibilities are,

$$\chi_p^P = \frac{N_g\sigma_{ge}^P}{\Omega_p} \tag{4}$$
$$= N_g \frac{i\gamma'_{gr}\gamma'_{ga}\gamma'_{gm}A_m^*\sigma_{gg}}{\gamma'_{gm}A_gA_m^* + \gamma'^*_{mr}\gamma'^*_{ma}A_g|\Omega_p|^2 + \gamma'_{gr}\gamma'_{ga}A_m^*|\Omega_t|^2}$$
$$\chi_t^P = \frac{N_m\sigma_{gm}^P}{\Omega_t} \tag{5}$$
$$= N_m \frac{i\gamma'_{mr}\gamma'_{ma}\gamma'_{mg}A_g^*\sigma_{mm}}{\gamma'_{mg}A_mA_g^* + \gamma'^*_{gr}\gamma'^*_{ga}A_m|\Omega_t|^2 + \gamma'_{mr}\gamma'_{ma}A_g^*|\Omega_p|^2},$$

where σ_{ge}^P and σ_{me}^P are steady-state solutions of Eq.s (3). We denote here by $N_g = N_0 d_{eg}^2/2\varepsilon_0\hbar$, $N_m = N_0 d_{em}^2/2\varepsilon_0\hbar$ and N_0 the average volume density of a finite atomic sample of length L. We also define $A_g = \gamma'_{gr}B_g + \gamma'_{ga}|\Omega_d|^2$ and $B_g = \gamma'_{ge}\gamma'_{ga} + |\Omega_c|^2$ as well as $A_m = \gamma'_{mr}B_m + \gamma'_{ma}|\Omega_d|^2$ and $B_m = \gamma'_{me}\gamma'_{ma} + |\Omega_c|^2$.

The inverted-Ψ configuration $(A1)$ can be seen as made of two *adjacent* inverted-Y configurations, one involving the probe field $(B1)$ and the other involving the trigger field $(C1)$, and both sharing the driving and coupling fields Ω_d and Ω_c. Each inverted-Y configuration has, in turn, double dark-states [36] whereby the *probe* field, for instance, exhibits double-EIT [3, 37, 38] leading to different transparency windows centered around $\delta_p = \delta_c$ and $\delta_p = -\delta_d$ with almost identical probe responses at both window centers. The two windows become centered at the same position when the dark states become degenerate, namely when $\delta_c \to -\delta_d$. Clearly, the same holds unchanged for the trigger response.

The inverted-Ψ configuration $(A1)$, owing to its intrinsic symmetric driving structure, further allows for tuning of these two pairs of dark-states and, in particular, for their matching. This takes place when $\Omega_p = \Omega_t$ and $\delta_p = \delta_t$ and gives rise to similar absorptive and dispersive properties, hence similar group velocities, for *both* probe and trigger fields. Note, in fact, that under such a *symmetric* EIT driving the two expressions for χ_p^P and χ_t^P turn into each another upon the interchange $\{g \leftrightarrow m, p \leftrightarrow t\}$ [39]. Matching, in addition, yields almost identical probe responses in both inverted-Ψ $(A1)$ and inverted-Y $(B1)$ configurations. Likewise for a trigger field driving the $(A1)$ and $(C1)$ configurations.

Owing to dipole blockade, level $|r\rangle$ may be decoupled, which reduces the inverted-Ψ configuration $(A1)$ to a tripod configuration $(A2)$ whose susceptibilities can easily be computed from Eqs. (3) by setting $\Omega_d = 0$, i.e.,

$$\chi_p^T = N_g \frac{i\gamma'_{ga}\gamma'_{gm}B_m^*\sigma_{gg}}{(\gamma'_{gm}B_g + \gamma'_{ga}|\Omega_t|^2)B_m^* + \gamma'^*_{ma}|\Omega_p|^2B_g} \tag{6}$$
$$\chi_t^T = N_m \frac{i\gamma'_{ma}\gamma'_{mg}B_g^*\sigma_{mm}}{(\gamma'_{mg}B_m + \gamma'_{ma}|\Omega_p|^2)B_g^* + \gamma'^*_{ga}|\Omega_t|^2B_m} \tag{7}$$

B. Polarizations $\{\sigma_p^+, \sigma_t^+\}$.

The probe susceptibility associated with this polarizations choice corresponds to an inverted-Y configuration ($B1$) obtained by setting $\Omega_t = 0$ in Eqs. (3),

$$\chi_p^Y = N_g \frac{i\gamma'_{gr}\gamma'_{ga}\sigma_{gg}}{A_g}, \tag{8}$$

which reduces, in the presence of dipole blockade ($\Omega_t = \Omega_d = 0$), to that of a lambda configuration ($B2$),

$$\chi_p^L = N_g \frac{i\gamma'_{ga}\sigma_{gg}}{\gamma'_{ge}\gamma'_{ga} + |\Omega_c|^2} \tag{9}$$

In this case the trigger susceptibility vanishes as in vacuum ($\chi_t^v = 0$).

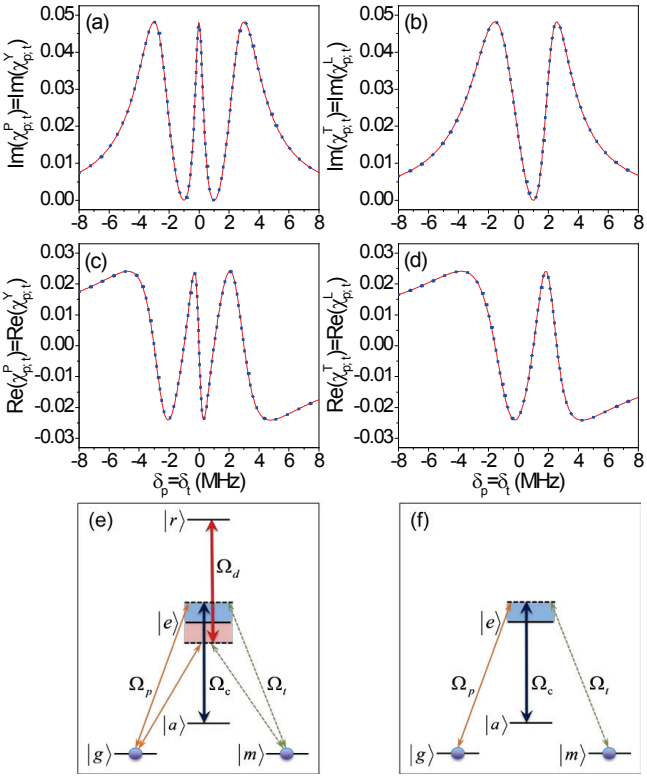

FIG. 2: (Color online) Imaginary (a,b) and real (c,d) parts of probe and trigger susceptibilities *vs.* probe and trigger detunings $\delta_p = \delta_t$ under *balanced driving* (*see text*) with $\sigma_{gg} = \sigma_{mm} = 0.5$ and $\Omega_p = \Omega_t = 3.0$ kHz. The susceptibility plotted in (a,c) refer to the inverted-Ψ (red-thin) and inverted-Y (blue-dotted) configurations whose relevant level transitions are shown schematically in panel (e). The susceptibility plotted in (b,d) refer to the tripod (red-thin) and lambda (blue-dotted) configurations with relevant level transitions shown schematically in panel (f). The coupling and dressing field parameters are $\Omega_c = \Omega_d = 2.0$ MHz, $\delta_c = \delta_d = 1.0$ MHz, while the atomic parameters are $\gamma_{ge} = \gamma_{me} = 3.0$ MHz, $\gamma_{gr} = \gamma_{mr} = 3.0$ kHz, $\gamma_{ga} = \gamma_{gm} = \gamma_{ma} = 1.0$ kHz, $d_{eg} = d_{em} = 1.5 \times 10^{-29}$ Cm, and $N_0 = 2.4 \times 10^{12}$ cm^{-3}.

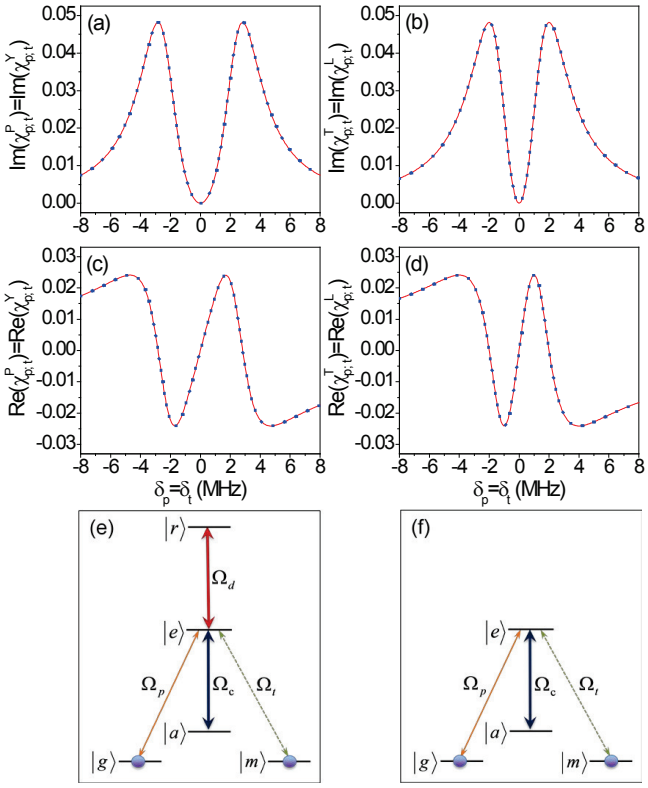

FIG. 3: (Color online.) Same as in Fig. 2 except that we take $\delta_c = \delta_d = 0$ here. The pair of probe (trigger) transparency windows now collapse into a single one centered at $\delta_p = \delta_t = 0$ (*see text*) for all configurations whose relevant level transitions are shown schematically in panels (e) and (f).

***C.* Polarizations** $\{\sigma_p^-,\ \sigma_t^-\}$. This is instead the reverse situation in which the probe field has a vanishing susceptibility ($\chi_p^v = 0$) while the trigger susceptibility corresponds to that of an inverted-Y configuration ($C1$),

$$\chi_t^Y = N_m \frac{i\gamma'_{mr}\gamma'_{ma}\sigma_{mm}}{B}, \tag{10}$$

or to that of a Lambda configuration ($C2$),

$$\chi_t^L = N_m \frac{i\gamma'_{ma}\sigma_{mm}}{\gamma'_{me}\gamma'_{ma} + |\Omega_c|^2}. \tag{11}$$

As before they are obtained from Eqs. (3) by setting, respectively, $\Omega_p = 0$ or $\Omega_p = \Omega_d = 0$.

The analytical results ($A \to C$) anticipated above are further discussed here through the direct computation of all relevant atomic susceptibilities. In Fig. 2 we plot both real and imaginary parts of the probe and trigger susceptibilities associated with all six level configurations shown in Fig. 1. We first observe that, under a symmetric EIT driving, the probe and trigger fields always exhibit identical susceptibilities whether we deal with an inverted-Ψ (red-thin) configuration ($A1$) or with an inverted-Y (blue-dotted) configuration ($B1$,$C1$), that is $\chi_p^P = \chi_t^P$ and $\chi_p^Y = \chi_t^Y$ as shown in Fig. 2(a,c). These two panels

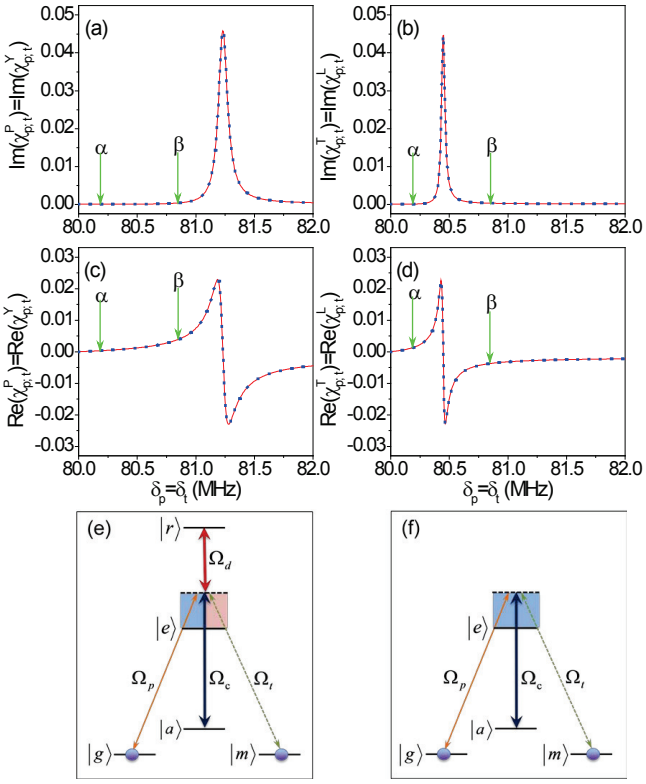

FIG. 4: (Color online) Same as in Fig. 2 except that we take $\delta_c = -\delta_d = 80.0$ MHz, $\Omega_c = 6.0$ MHz, and $\Omega_d = 8.0$ MHz. The pair of probe (trigger) transparency windows now collapse into a single one (*see text*) centered at $\delta_p = \delta_t = 80.0$ MHz for all configurations. The two points 'α' and 'β' denote two different reference detunings used in Sect. V.

further show that the *probe* absorption and dispersion are nearly indistinguishable for an inverted-Ψ (*A1*) as well as for an inverted-Y (*B1,C1*) configuration, that is $\chi_p^P \simeq \chi_p^Y$. In the same way this holds for the *trigger* field, with $\chi_t^P \simeq \chi_t^Y$. At variance with refs. [9, 14, 36], where slightly different probe and trigger detunings are needed to balance their absorption and dispersion responses, our probe and trigger fields interact in a *symmetric* configuration with identical frequencies and amplitudes. Identical probe and trigger absorption and dispersion are then *intrinsic* to our model.

Fig. 2(a) displays the typical *double-EIT* spectrum with two probe (trigger) transparency windows placed at $\delta_p = \delta_c = 1.0$ MHz and $\delta_p = -\delta_d = -1.0$ MHz and this occurs for *both* inverted-Ψ and inverted-Y configurations in the non-degenerate near-resonant EIT regime. One transparency window ($\delta_p = \delta_c = 1.0$ MHz) opens up as due to the interaction between the longer probe (trigger) leg and the coupling beam whereas the other window ($\delta_p = -\delta_t = -1.0$ MHz) arises as due to the interaction of the shorter probe (trigger) leg and the dressing beam as depicted in Fig. 2(e). Such a double-window structure clearly disappears in the presence of dipole Rydberg blockade effects when the three configurations (*A1-C1*) reduce respectively to the three configurations (*A2-C2*) (see Fig. 2(f)). This is observed in Fig. 2(b,d) where the probe (trigger) susceptibility in the tripod (red-thin) and lambda (blue-dotted) configurations clearly exhibits the typical *single-EIT* spectrum with only one window left at $\delta_p = \delta_c = 1.0$ MHz. The two equalities mentioned above still hold for tripod and lambda configurations, namely $\chi_p^{T,L} = \chi_t^{T,L}$ and $\chi_{p,t}^T \simeq \chi_{p,t}^L$.

Fig. 3 is plotted instead for $\delta_c = \delta_d = 0$ (degenerate resonant double-EIT regime) in which case the two transparency windows collapse into a single one. Notice that in this case the EIT window associated with the two inverted-Ψ and inverted-Y configurations is slightly wider than the one observed for the tripod and lambda configurations. Finally, we consider the degenerate far-detuned double-EIT case attained with $\delta_c = 80$ MHz and $\delta_d = -80$ MHz. We show in Fig. 4 the absorption line to the right of the center of the transparency window at $\delta_p = \delta_t = 80.0$ MHz, on a spectral range of detunings of interest for the cross-phase modulation effects discussed in Sect.V. In particular, two specific choices of detuning will be considered below and indicated by the points 'α' and 'β' in Fig. 4. Such detunings are on the same side of this absorption line [Fig. 4(a,c))] for the inverted-Ψ and inverted-Y configurations. For the corresponding tripod and lambda configurations, instead, the points 'α' and 'β' are placed on opposite sides with respect to the absorption peak [Fig. 4(b,d)] because the width of the transparency window is reduced as the driving field is decoupled ($\Omega_d \to 0$). The 'α' and 'β' detunings will be chosen in Sect. V to optimize polarization selective cross-phase modulation effects respectively in long ($L = 2.0$ mm) and short ($L = 0.1$ mm) samples, while minimizing the losses.

IV. SA RYDBERG POPULATIONS

For given polarizations of probe and trigger fields, cold ^{87}Rb atoms under consideration behave in principle as a combination of inverted-Ψ and tripod EIT systems (*A1* $\leftrightarrow$ *A2*) or a combination of inverted-Y and lambda EIT systems (*B1* $\leftrightarrow$ *B2* and *C1* $\leftrightarrow$ *C2*). Such a correlation of level configurations depends critically on dipole blockade of Rydberg excitations, which can be quantified by SA Rydberg populations as discussed below.

Now we transfer to the language of so-called SAs. Each SA is defined by the $n_{SA} \simeq 4\pi N_0 R_b^3/3$ atoms inside a blockade sphere of the radius [40]

$$R_b \simeq \left(\frac{|\Delta_d|\, C_6}{|\Omega_c|^2 + |\Omega_d|^2}\right)^{1/6} \quad \text{for} \quad |\Delta_d| \gg \gamma_{ge} = \gamma_{me}\ ,$$

$$R_b \simeq \left(\frac{\gamma_{ge}\, C_6}{|\Omega_c|^2 + |\Omega_d|^2}\right)^{1/6} \quad \text{for} \quad |\Delta_d| \ll \gamma_{ge} = \gamma_{me}\ ,$$

where the van der Waals (vdW) coefficient C_6 depends on the principal quantum number n of Rydberg level $|r\rangle$

with $C_6 = n^{11}(c_0+c_1n+c_2n^2)$ for the $ns-ns$ asymptotes of cold ^{87}Rb atoms [41]. Using $C_6 = -1.67\times10^{13}$ s^{-1} μm^6 for $n = 90$, $\Delta_d = 80$ MHz, $\Omega_c = 6.0$ MHz, $\Omega_d = 8.0$ MHz, and $N_0 = 2.4\times10^{12}$ cm^{-3}, it is easy to find that the blockade radius is $R_b \simeq 15.4$ μm and the atomic number is $n_{SA} \simeq 36700$ for a given SA [42].

***A*. Polarizations $\{\sigma_p^+, \sigma_t^-\}$.**

When the probe and trigger fields exhibit σ_p^+ and σ_t^- polarizations, SAs should be described by the ground collective states $|G\rangle = \left|g_1, g_2, ..., g_{n_{SA}/2}\right\rangle$ and $|M\rangle = \left|m_1, m_2, ..., m_{n_{SA}/2}\right\rangle$ as well as the first-order excited collective states $\left|A^1\right\rangle = (\left|A^{1g}\right\rangle + \left|A^{1m}\right\rangle)/\sqrt{2}$, $\left|E^1\right\rangle = (\left|E^{1g}\right\rangle + \left|E^{1m}\right\rangle)/\sqrt{2}$, and $\left|R^1\right\rangle = (\left|R^{1g}\right\rangle + \left|R^{1m}\right\rangle)/\sqrt{2}$ with the following six components

$$\begin{aligned}
\left|R^{1g}\right\rangle &= \sqrt{\frac{2}{n_{SA}}} \times \textstyle\sum_{j=1}^{n_{SA}/2} \left|g_1, g_2, ..., r_j, ..., g_{n_{SA}/2}\right\rangle \\
\left|E^{1g}\right\rangle &= \sqrt{\frac{2}{n_{SA}}} \times \textstyle\sum_{j=1}^{n_{SA}/2} \left|g_1, g_2, ..., e_j, ..., g_{n_{SA}/2}\right\rangle \\
\left|A^{1g}\right\rangle &= \sqrt{\frac{2}{n_{SA}}} \times \textstyle\sum_{j=1}^{n_{SA}/2} \left|g_1, g_2, ..., a_j, ..., g_{n_{SA}/2}\right\rangle \\
\left|R^{1m}\right\rangle &= \sqrt{\frac{2}{n_{SA}}} \times \textstyle\sum_{j=1}^{n_{SA}/2} \left|m_1, m_2, ..., r_j, ..., m_{n_{SA}/2}\right\rangle \\
\left|E^{1m}\right\rangle &= \sqrt{\frac{2}{n_{SA}}} \times \textstyle\sum_{j=1}^{n_{SA}/2} \left|m_1, m_2, ..., e_j, ..., m_{n_{SA}/2}\right\rangle \\
\left|A^{1m}\right\rangle &= \sqrt{\frac{2}{n_{SA}}} \times \textstyle\sum_{j=1}^{n_{SA}/2} \left|m_1, m_2, ..., a_j, ..., m_{n_{SA}/2}\right\rangle
\end{aligned}$$

while other higher-order excited collective states (with more than one atoms at level $|r\rangle$ or level $|a\rangle$) can be neglected near the EIT window center [35].

The SA operators $\Sigma_{ij} = |I\rangle\langle J|$ obey similar dynamic equations as those for atomic operators $\sigma_{ij} = |i\rangle\langle j|$ except that the probe and trigger Rabi frequencies should be respectively replaced by [43]

$$\Omega_p \to \Omega_p^s = \sqrt{\frac{n_{SA}}{2}}\ \Omega_p \qquad \Omega_t \to \Omega_t^s = \sqrt{\frac{n_{SA}}{2}}\ \Omega_t. \quad (12)$$

That is, the collective transitions $|G\rangle \leftrightarrow \left|E^{1g}\right\rangle$ and $|M\rangle \leftrightarrow \left|E^{1m}\right\rangle$ are enhanced to have respectively Rabi frequencies Ω_p^s and Ω_t^s, which may be comparable to Ω_c and Ω_d even if $\Omega_{p,t} \ll \Omega_{c,d}$. Note, however, that dipole-dipole interactions may result in the modification of two-particle quantum correlations. As a matter of fact [30], $\Omega_{p,t}^2$ should be further replaced by $\Omega_{p,t}^2 g_{p,t}$ to include two-photon correlations

$$g_{p,t} = \frac{\left\langle \hat{\Omega}_{p,t}^\dagger \hat{\Omega}_{p,t}^\dagger \hat{\Omega}_{p,t} \hat{\Omega}_{p,t} \right\rangle}{\left\langle \hat{\Omega}_{p,t}^\dagger \hat{\Omega}_{p,t} \right\rangle^2} \quad (13)$$

quantifying the probability of having at least two photons in a blockade volume, but we have $g_{p,t} \to 1.0$ near the center of a degenerate EIT window at $\delta_{p,t} = -\delta_d = \delta_c$ with $|\delta_{c,d}| \gg \gamma_{ge}$ when the input probe and trigger fields are in *coherent* states [35]. Thus we obtain from Eqs. (3)

$$\begin{aligned}
\partial_t \Sigma_{ge}^P &= -\gamma'_{ge}\Sigma_{ge}^P + i\Omega_d^*\Sigma_{gr}^P + i\Omega_c\Sigma_{ga}^P + i\Omega_t^s\Sigma_{gm}^P + i\Omega_p^s\Sigma_{gg}^P \\
\partial_t \Sigma_{ga}^P &= -\gamma'_{ga}\Sigma_{ga}^P + i\Omega_c^*\Sigma_{ge}^P \\
\partial_t \Sigma_{gr}^P &= -\gamma'_{gr}\Sigma_{gr}^P + i\Omega_d\Sigma_{ge}^P \\
\partial_t \Sigma_{me}^P &= -\gamma'_{me}\Sigma_{me}^P + i\Omega_d^*\Sigma_{mr}^P + i\Omega_c\Sigma_{ma}^P + i\Omega_p^s\Sigma_{mg}^P + i\Omega_t^s\Sigma_{mm}^P \\
\partial_t \Sigma_{ma}^P &= -\gamma'_{ma}\Sigma_{ma}^P + i\Omega_c^*\Sigma_{me}^P \\
\partial_t \Sigma_{mr}^P &= -\gamma'_{mr}\Sigma_{mr}^P + i\Omega_d\Sigma_{me}^P \\
\partial_t \Sigma_{gm}^P &= -\gamma'_{gm}\Sigma_{gm}^P + i\Omega_t^{s\dagger}\Sigma_{ge}^P - i\Omega_p^s\Sigma_{em}^P
\end{aligned} \quad (14)$$

for the inverted-Ψ double-EIT system. To solve Eqs. (14) in the steady state, we should first express Σ_{gg}^P and Σ_{mm}^P in terms of the variables Σ_{ij}^P and three considerations are now in order. *First*, we recall that

$$\Sigma_{aa}^P = \Sigma_{aa}^{gP} + \Sigma_{aa}^{mP} = \frac{\Sigma_{ag}^P\Sigma_{ga}^P}{\Sigma_{gg}^P} + \frac{\Sigma_{am}^P\Sigma_{ma}^P}{\Sigma_{mm}^P}\ ,$$

$$\Sigma_{ee}^P = \Sigma_{ee}^{gP} + \Sigma_{ee}^{mP} = \frac{\Sigma_{eg}^P\Sigma_{ge}^P}{\Sigma_{gg}^P} + \frac{\Sigma_{em}^P\Sigma_{me}^P}{\Sigma_{mm}^P}\ ,$$

$$\Sigma_{rr}^P = \Sigma_{rr}^{gP} + \Sigma_{rr}^{mP} = \frac{\Sigma_{rg}^P\Sigma_{gr}^P}{\Sigma_{gg}^P} + \frac{\Sigma_{rm}^P\Sigma_{mr}^P}{\Sigma_{mm}^P}\ .$$

and *second* we notice that Σ_{aa}^P and Σ_{rr}^P may be comparable to Σ_{gg}^P and Σ_{mm}^P, as a result of enhanced collective transitions, whereas Σ_{ee}^P is negligible owing to quantum destructive interference in the EIT regime. In fact, $\Sigma_{aa}^{gP}/\Sigma_{rr}^{gP} \approx \Omega_c^2/\Omega_d^2$ and $\Sigma_{ee}^{gP}/\Sigma_{rr}^{gP} \approx \gamma_{gr}^2/\Omega_d^2$ in the two-photon near-resonant case of $|\Delta_{a,r}| \ll \Omega_{c,d}$ as well as $\Sigma_{aa}^{mP}/\Sigma_{rr}^{mP} \approx \Omega_c^2/\Omega_d^2$ and $\Sigma_{ee}^{mP}/\Sigma_{rr}^{mP} \approx \gamma_{mr}^2/\Omega_d^2$ in the

two-photon near-resonant case of $|\Delta'_{a,r}| \ll \Omega_{c,d}$, as follows from Eqs. (14) in the steady state. *Third*, notice that $\Sigma^{gP}_{rr} + \Sigma^{gP}_{aa} + \Sigma^{P}_{gg} = 0.5$ and $\Sigma^{mP}_{rr} + \Sigma^{mP}_{aa} + \Sigma^{P}_{mm} = 0.5$ in a good approximation for the boundary conditions $\Omega_p(z=0) = \Omega_t(z=0)$ and initial conditions $\Sigma_{gg}(t=0) = \Sigma_{mm}(t=0)$, as follows from the second consideration and the conservation of the SA population. From all the above we obtain,

$$\Sigma^{P}_{gg} = \frac{1}{4} + \frac{1}{4}\sqrt{1 - 16(\Sigma^{P}_{rg}\Sigma^{P}_{gr} + \Sigma^{P}_{ag}\Sigma^{P}_{ga})} \qquad (15)$$
$$\Sigma^{P}_{mm} = \frac{1}{4} + \frac{1}{4}\sqrt{1 - 16(\Sigma^{P}_{rm}\Sigma^{P}_{mr} + \Sigma^{P}_{am}\Sigma^{P}_{ma})} \quad .$$

which are then used to solve Eqs. (14) upon setting $\partial_t \Sigma^{P}_{ij} = 0$ to arrive at the following steady state SA Rydberg populations

$$\Sigma^{gP}_{rr} = \frac{0.5|\gamma'_{ga}|^2|\Omega^s_p|^2|\Omega_d|^2}{|A_g + \gamma'^{*}_{mr}(\gamma'^{*}_{ma}/\gamma'_{gm})|\Omega^s_p|^2(A_g/A^*_m) + \gamma'_{gr}(\gamma'_{ga}/\gamma'_{gm})|\Omega^s_t|^2|^2 + (\gamma'^2_{ga}|\Omega_d|^2 + \gamma'^2_{gr}|\Omega_c|^2)|\Omega^s_p|^2}$$
$$\Sigma^{mP}_{rr} = \frac{0.5|\gamma'_{ma}|^2|\Omega^s_t|^2|\Omega_d|^2}{|A_m + \gamma'^{*}_{gr}(\gamma'^{*}_{ga}/\gamma'_{mg})|\Omega^s_t|^2(A_m/A^*_g) + \gamma'_{mr}(\gamma'_{ma}/\gamma'_{mg})|\Omega^s_p|^2|^2 + (\gamma'^2_{ma}|\Omega_d|^2 + \gamma'^2_{mr}|\Omega_c|^2)|\Omega^s_t|^2} \qquad (16)$$

for the inverted-Ψ double-EIT system.

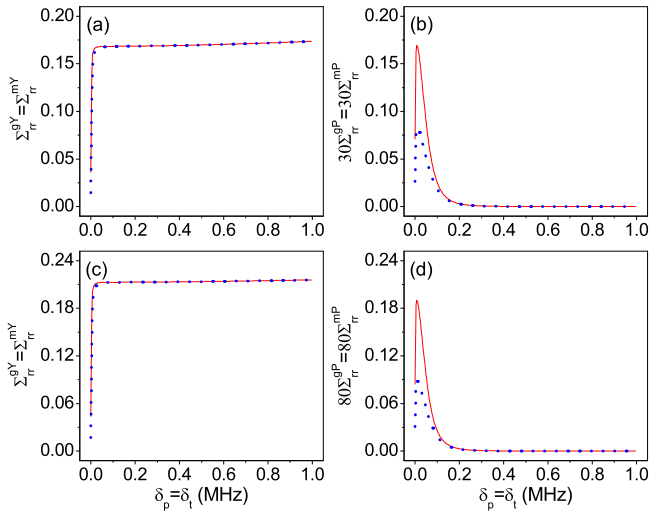

FIG. 5: (Color online) Rydberg populations of SAs for the inverted-Y (a,c) and inverted-Ψ (b,d) configurations in the degenerate resonant double-EIT regime with $\delta_c = -\delta_d = 0$. Red-thin and blue-dotted curves correspond, respectively, to $\gamma_{gr} = \gamma_{mr} = 3.0$ kHz and $\gamma_{gr} = \gamma_{mr} = 5.0$ kHz. Other parameters are the same as in Fig. 3 except $\Omega_p = \Omega_t = 30$ kHz in panels (a,b); $\Omega_p = \Omega_t = 50$ kHz in panels (c,d).

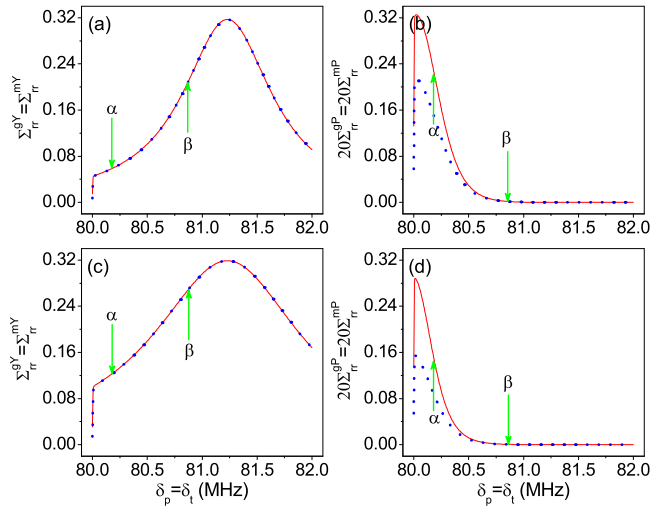

FIG. 6: (Color online) Rydberg populations of SAs for the inverted-Y (a,c) and inverted-Ψ (b,d) configurations in the degenerate far-detuned double-EIT regime with $\delta_c = -\delta_d = 80$ MHz. Red-thin and blue-dotted curves refer, respectively, to $\gamma_{gr} = \gamma_{mr} = 3.0$ kHz and $\gamma_{gr} = \gamma_{mr} = 5.0$ kHz. Other parameters are the same as in Fig. 4 except $\Omega_p = \Omega_t = 30$ kHz in panels (a,b); $\Omega_p = \Omega_t = 50$ kHz in panels (c,d).

B. Polarizations $\{\sigma^+_p, \sigma^+_t\}$ ($\{\sigma^-_p, \sigma^-_t\}$).

When the probe and trigger fields exhibit σ^+_p and σ^+_t (or σ^-_p and σ^-_t) polarizations, SAs are described by the collective states $|G\rangle$, $|A^{1g}\rangle$, $|E^{1g}\rangle$, and $|R^{1g}\rangle$ (or $|M\rangle$, $|A^{1m}\rangle$, $|E^{1m}\rangle$, and $|R^{1m}\rangle$) in the *inverted*-Y configuration. In this case, relevant SA Liouville equations can be derived by setting $\Omega^s_t = 0$ or $\Omega^s_p = 0$ in Eqs. (14). Then with similar considerations mentioned above, we obtain

the following SA Rydberg populations

$$\Sigma_{rr}^{gY} = \frac{0.5|\gamma'_{ga}|^2|\Omega_p^s|^2|\Omega_d|^2}{|A_g|^2 + (|\gamma'_{ga}|^2|\Omega_d|^2 + |\gamma'_{gr}|^2|\Omega_c|^2)|\Omega_p^s|^2} \quad (17)$$

$$\Sigma_{rr}^{mY} = \frac{0.5|\gamma'_{ma}|^2|\Omega_t^s|^2|\Omega_d|^2}{|A_m|^2 + (|\gamma'_{ma}|^2|\Omega_d|^2 + |\gamma'_{mr}|^2|\Omega_c|^2)|\Omega_t^s|^2}$$

for the inverted-Y double-EIT systems. In a good approximation, they are restricted by $\Sigma_{rr}^{gY}+\Sigma_{aa}^{gY}+\Sigma_{gg}^{Y} = 0.5$ and $\Sigma_{rr}^{mY} + \Sigma_{aa}^{mY} + \Sigma_{mm}^{Y} = 0.5$, respectively.

In Fig. 5 and Fig. 6, we plot SA Rydberg populations in the inverted-Ψ and inverted-Y configurations as a function of probe and trigger detunings $\delta_p = \delta_t$, for realistic values of $\Omega_p = \Omega_t$ and of $\gamma_{gr} = \gamma_{mr}$. Fig. 5 is attained in the degenerate resonant EIT regime with $\delta_c = -\delta_d = 0$ while Fig. 6 is attained in the degenerate far-detuned EIT regime with $\delta_c = -\delta_d = 80$ MHz. We observe a remarkable difference of SA Rydberg populations $\Sigma_{rr}^{gP} - \Sigma_{rr}^{gY}$ ($\Sigma_{rr}^{mP} - \Sigma_{rr}^{mY}$) even if $\Omega_{p,t} \ll \Omega_{c,d}$ since it is possible to have $\Omega_{p,t}^s \sim \Omega_{c,d}$ in a dense enough sample. We also observe $\Sigma_{rr}^{gY} = \Sigma_{rr}^{mY} \gg \Sigma_{rr}^{gP} = \Sigma_{rr}^{mP}$, indicating that SA Rydberg excitations are large when only the probe or trigger field is coupled to the $|e\rangle$ level, while they are suppressed when both probe and trigger fields are coupled to the $|e\rangle$ level. This is a salient result as it prompts a large difference between the SA Rydberg populations respectively in the inverted-Ψ and inverted-Y configurations, which might be exploited to attain large conditional phase shifts [44, 45]. Such a suppression basically arises from the facts that (i) the collective SA transition amplitudes $|G\rangle \leftrightarrow |E^{1g}\rangle$ and $|M\rangle \leftrightarrow |E^{1m}\rangle$ are both enhanced by the large factor $\sqrt{n_{sa}/2}$ and (ii) in the symmetric inverted-Ψ configuration ($A1$) the two transition pathways *interfere* destructively yielding a greatly suppressed Rydberg population compared to those attained by excitation through the asymmetric inverted-Y configurations ($B1$ and $C1$), encompassing instead only a single transition amplitude.

It should be finally noticed that in the limit of weak probe and trigger fields, even when dipole blockade is effective, the actual fraction of atoms in levels different from $|g\rangle$ and $|m\rangle$ remains very small: even for SA Rydberg populations of order 1 as in Fig. 5 and Fig. 6, $\sigma_{ee} < \sigma_{aa} \sim \sigma_{rr} < 10^{-4}$ as $n_{SA} > 30000$. Then, heating of the sample due to absorption of coupling and dressing fields is strongly suppressed as both coupling and dressing fields interact with nearly empty levels.

V. RYDBERG COOPERATIVE NONLINEARITIES

With the individual susceptibilities of Sect. III and the superatom populations of Sect. IV, we now examine the dispersion and absorption properties exhibited by a pair of *monochromatic* probe and trigger fields traveling through an atomic sample under the three different polarization configurations of Fig. 1. For each of the correlated EIT regimes $A1 \leftrightarrow A2$, $B1 \leftrightarrow B2$, and $C1 \leftrightarrow C2$, the susceptibilities can be written as,

$$\chi_p^a = 2\Sigma_{rr}^{gP}\chi_p^T + (1 - 2\Sigma_{rr}^{gP})\chi_p^P \qquad for \quad \left\{\sigma_p^+ \quad \& \quad \sigma_t^-\right\} \quad (18)$$

$$\chi_t^a = 2\Sigma_{rr}^{mP}\chi_t^T + (1 - 2\Sigma_{rr}^{mP})\chi_t^P \qquad for \quad \left\{\sigma_p^+ \quad \& \quad \sigma_t^-\right\} \quad (19)$$

$$\chi_p^b = 2\Sigma_{rr}^{gY}\chi_p^L + (1 - 2\Sigma_{rr}^{gY})\chi_p^Y \qquad for \quad \left\{\sigma_p^+ \quad \& \quad \sigma_t^+\right\} \quad (20)$$

$$\chi_t^c = 2\Sigma_{rr}^{mY}\chi_t^L + (1 - 2\Sigma_{rr}^{mY})\chi_{tt}^Y \qquad for \quad \left\{\sigma_p^- \quad \& \quad \sigma_t^-\right\}, \quad (21)$$

clearly showing cooperative dispersion and absorption effects depending on whether or not the ensemble is optically driven into the Rydberg state (*dipole blockade*). **The concept of an excitation blockade sphere, adopted here [46] to get an intuitive physical picture of the effects of the dipole-dipole interaction on the probe and trigger coherences (2), enables one to include the Rydberg blockade effects in the average atomic susceptibilities (18-21) which will then be used to describe the optical response of the entire sample.** A monochromatic *probe* impinging **over a sample of length L** with a vacuum wave-vector k_p experiences, *e.g.*, the phase shift

$$\phi_p^{a,b} = \mathrm{Re}(\chi_p^{a,b})k_pL/2, \quad (22)$$

whereas the extinction coefficient is

$$\kappa_p^{a,b} = \mathrm{Im}(\chi_p^{a,b})k_pL/2. \quad (23)$$

Similar expressions for $\phi_t^{a,c}$ and $\kappa_t^{a,c}$ hold for the *trigger* upon replacing $p \to t$ in the above equations. Because the susceptibilities $\chi_{p;t}^P$ ($\chi_{p;t}^T$) and $\chi_{p;t}^Y$ ($\chi_{p;t}^L$) are indistinguishable (see Fig. 4) and the populations Σ_{rr}^{gP} (Σ_{rr}^{mP}) and Σ_{rr}^{gY} (Σ_{rr}^{mY}) are in general very different (see Fig. 6),

we expect that ϕ_p^a (κ_p^a) be different from ϕ_p^b (κ_p^b) and likewise ϕ_t^a (κ_t^a) be different from ϕ_t^c (κ_t^c). Such departures are then a direct manifestation of the cooperative nonlinearities arising from the dipole Rydberg blockade. When Rydberg transitions are involved, in fact, the steady-state optical response, hence the phase shifts and absorption, will also depend on the probability to find an atom excited into the Rydberg state.

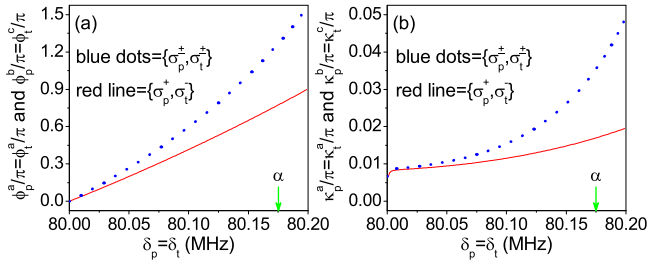

FIG. 7: (Color online) Cooperative phase shifts (a) and extinction constants (b) acquired over a $L = 2.0$ mm long sample around the point 'α' [Fig. 4] under the inverted-Ψ (*A1*) (*red-thin line*) and under the inverted-Y (*B1*, *C1*) (*blue-dotted line*) EIT configurations. Here $\gamma_{gr} = \gamma_{mr} = 3.0$ kHz and $\Omega_p = \Omega_t = 50$ kHz while other parameters are the same as in Fig. 6.

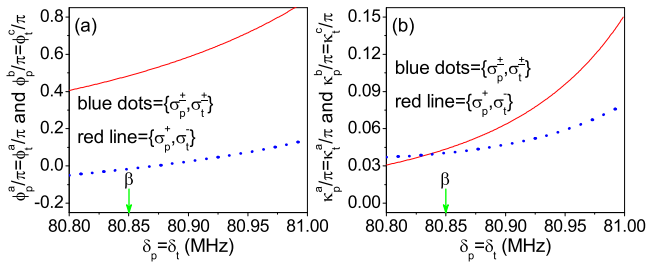

FIG. 8: (Color online) Same as in Fig. 7 for shifts (a) and extinctions acquired over a $L = 0.1$ mm sample around the point 'β' [Fig. 4]

We plot in Fig. 7 and Fig. 8 the cooperative phase shifts $\phi_p^{a,b} = \phi_t^{a,c}$ and extinction coefficients $\kappa_p^{a,b} = \kappa_t^{a,c}$ as a function of probe and trigger detunings $\delta_p = \delta_t$. This is done respectively for a long sample ($L = 2.0$ mm) containing 65 SAs around point 'α' and for a short sample ($L = 0.1$ mm) containing *only* about 3 SAs around point 'β' in the degenerate far-detuned regime with $\delta_c = -\delta_d = 80$ MHz [Fig. 4,6]. We can reach $\phi_p^a = \phi_t^a = 0.77\pi$ and $\phi_p^b = \phi_t^c = 1.27\pi$, with $\kappa_p^a = \kappa_t^a \approx 0.02\pi$ and $\kappa_p^b = \kappa_t^c \approx 0.04\pi$ at $\delta_p = \delta_t \approx 80.17$ MHz (point 'α') in Fig. 7. We further observe $\phi_p^a = \phi_t^a = 0.48\pi$ and $\phi_p^b = \phi_t^c = -0.01\pi$ with $\kappa_p^a = \kappa_t^a \approx 0.04\pi$ and $\kappa_p^b = \kappa_t^c \approx 0.04\pi$ at $\delta_p = \delta_t \approx 80.850$ MHz (point 'β') in Fig. 8.

The cooperative nonlinearity arising from the Rydberg blockade may finally be compared with those arising from standard cross-Kerr EIT processes [2–4, 36] and to this

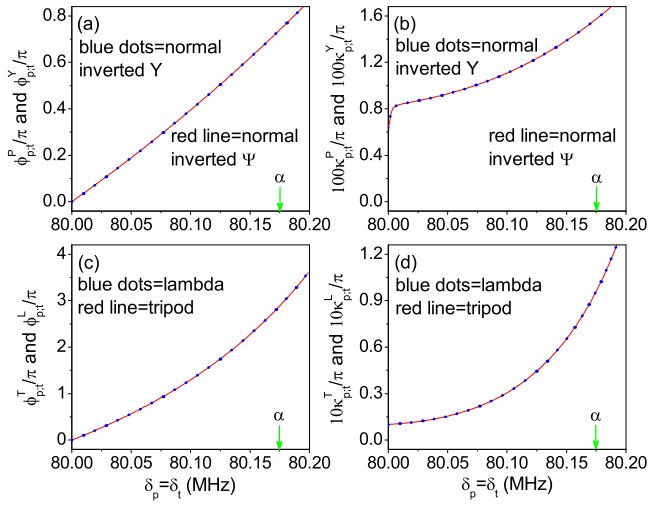

FIG. 9: (Color online) Same as same in Fig. 7 with cooperative phase shifts (a) and extinctions (b) acquired under the inverted-Ψ (*A1*) (*red-thin line*) and inverted-Y (*B1*, *C1*) (*blue-dotted line*) EIT configurations, with $|r\rangle$ being a *normal* excited state. Shifts (c) and extinctions (d) acquired under a tripod (*A2*) (*red-thin line*) and Lambda (*B2*, *C2*) (*blue-dotted line*) EIT configurations. Parameters and notation as in Fig. 7.

extent we examine two specific cases. We take (i) a sample driven in the inverted-Ψ and inverted-Y double-EIT configurations, yet with $|r\rangle$ being a *normal* excited level and (ii) a sample driven in the tripod and lambda single-EIT configurations. In the case (i), the probe and trigger phase shifts reduce to $\phi_{p,t}^P = \mathrm{Re}(\chi_{p,t}^P)k_{p,t}L/2$ and $\phi_{p,t}^Y = \mathrm{Re}(\chi_{p,t}^Y)k_{p,t}L/2$ while the extinction constants reduce to $\kappa_{p,t}^P = \mathrm{Im}(\chi_{p,t}^P)k_{p,t}L/2$ and $\kappa_{p,t}^Y = \mathrm{Im}(\chi_{p,t}^Y)k_{p,t}L/2$. In the case (ii), on the other hand, we have for the phase shifts $\phi_{p,t}^T = \mathrm{Re}(\chi_{p,t}^T)k_{p,t}L/2$ and $\phi_{p,t}^L = \mathrm{Re}(\chi_{p,t}^L)k_{p,t}L/2$ and for the extinction constants $\kappa_{p,t}^T = \mathrm{Im}(\chi_{p,t}^T)k_{p,t}L/2$ and $\kappa_{p,t}^L = \mathrm{Im}(\chi_{p,t}^L)k_{p,t}L/2$. This is shown in Fig. 9 where we use the same parameters as in Fig. 7 and plot in the left (right) panels the individual phase shifts $\phi_p^{P,Y} = \phi_t^{P,Y}$ ($\phi_p^{T,L} = \phi_t^{T,L}$) and individual extinction constants $\kappa_p^{P,Y} = \kappa_t^{P,Y}$ ($\kappa_p^{T,L} = \kappa_t^{T,L}$) around point '$\alpha$' [48]. Similar levels of absorptive losses and of (absolute) phase shifts are observed in Fig. 9. Yet unlike in Fig. 7, there are no appreciable differences between the two choices $\{\sigma_p^+, \sigma_t^-\}$ (*both* probe and trigger coupled) and $\{\sigma_p^\pm, \sigma_t^\pm\}$ (*either* probe or trigger coupled) for probe and trigger polarizations. This indicates that the conditional Rydberg blockade can be exploited to attain cross-phase modulation efficiencies that cannot be achieved at all with the usual Kerr-EIT nonlinearities that we examined in Fig. 9.

VI. CONCLUSIONS

A pair of weak probe and trigger fields interacting with a pair of strong coupling and dressing fields through a dense sample of cold rubidium atoms that may be driven to a Rydberg state can experience diverse regimes of electromagnetically induced transparency (EIT) depending on (a) the probe and trigger polarizations and (b) the presence of Rydberg blockade effects. This hinges on the probe and trigger circular *polarization selection* rules and on the *strength* of the linearly polarized coupling and driving fields, a most relevant instance of which is illustrated in the five-level inverted-Ψ EIT configuration ($A1$) of Fig. 1. The optical response in this configuration is central to this work and enables us, in turn, to readily compute the optical responses of other (reduced) EIT configurations such as, e.g., inverted-Y, tripod, and lambda (Sect. III). In each of these EIT configurations, whether Rydberg blockade is present or not, the probe and trigger propagation can be engineered so as to occur without significant absorption and dispersion. Depending on the choice of circular polarizations, on the other hand, probe and trigger cooperative *cross* nonlinear interactions originating from the Rydberg blockade become much stronger than those observed in typical Kerr-EIT media at the same level of linear absorption and dispersion [2–4, 36].

Our inverted-Ψ configuration, characterized by large *polarization conditional* nonlinear interactions between two weak optical fields with little absorption and dispersion, allows for efficient cross-phase modulation effects. The required conditions are (i) a *degenerate* EIT regime ($\delta_c = -\delta_d$) with large enough coupling and dressing fields ($\Omega_{c,d} \sim \gamma_{ge} \sim \gamma_{me}$), ($ii$) *far off resonant* probe and trigger EIT windows ($\delta_p = \delta_t = \delta_c = -\delta_d$=80 MHz, in our case) to guarantee that the two-photon correlation functions $g_p \approx g_t \approx$1, and finally (iii) *symmetric driving* with equally populated grounds $|g\rangle$ and $|m\rangle$. The last requirement is not only beneficial to achieve probe and trigger fields matching but also to ensure a suppression of the Rydberg population for the polarization choice of Fig. 1(A), in comparison with those of Fig. 1(B) and Fig. 1(C). One key advantage of our scheme is that Rydberg blockade results in the conditional reduction from a double EIT configuration to a simple EIT one, rather than to an absorbing one. This is the critical point for suppressing linear absorption and dispersion for any choices of probe and trigger polarizations.

The scheme we propose appears as a promising tool to implement a variety of all-optical polarization sensitive cross-phase nonlinearities with (polarization) conditional shifts of the order π. Dipole blockade depends on the probe and trigger polarization states with the inverted-Ψ and inverted-Y configurations exhibiting in fact quite different SA Rydberg populations. In particular, the scheme we propose could provide the basic physical mechanism for a universal vector gate [14] in which the nearly lossless and distorsionless propagation of probe and trigger pulses would be naturally matched thanks to the symmetry of our configuration. Large values of phase shift could be attained not only in samples containing only a few Rb superatoms, but also employing very weak pulses. We anticipate that cross phase shifts of order π might be achieved with pulses containing only a few hundreds of photons, the reason being that the variation of superatom Rydberg populations is mainly determined by $n_{sa}\,\Omega_{p,t}^2$ so that small Rabi frequencies $\Omega_{p,t}$ may be compensated by a large number n_{sa} of atoms per blockade sphere.

Acknowledgments

This work is supported by the National Nature Science Foundation (No. 11174110 and No. 61378094), the National Basic Research Program (No. 2011CB921603), and the 111 Project (No. B13013) of China. Jin-Hui Wu would like to acknowledge the kind hospitality of Scuola Normale Superiore at Pisa.

[1] P. Kok, W. J. Munro, K. Nemoto, T. C. Ralph, J. P. Dowling, and G. J. Milburn, Rev. Mod. Phys. **79**, 135-174 (2007).
[2] H. Schmidt and A. Imamoglu, Opt. Lett. **21**, 1936-1938 (2005).
[3] S.-J. Li, X.-D. Yang, X.-M. Cao, C.-H. Zhang, C.-D. Xie, and H. Wang, Phys. Rev. Lett. 101, 073602 (2008).
[4] B.-W. Shiau, M.-C. Wu, C.-C. Lin, and Y.-C. Chen, Phys. Rev. Lett. **106**, 193006 (2011).
000).
[5] M. Fleischhauer, A. Imamoglu, and J. P. Marangos, Rev. Mod. Phys. **77**, 633-673 (2005).
[6] S. E. Harris and L.V. Hau, Phys. Rev. Lett. **82**, 4611 (1999).
[7] R.B. Li, L. Deng ans E.W. Hagley Phys. Rev. Lett. **110**, 113902 (2013).
[8] M. D. Lukin and A. Imamoglu Phys. Rev. Lett. **84**, 1419 (2
[9] S. Rebic, D. Vitali, C. Ottaviani, P. Tombesi, M. Artoni, F. Cataliotti, and R. Corbalan, Phys. Rev. A **70**, 032317 (2004).
[10] D. Petrosyan and Gershon Kurizki, Phys. Rev. A 65, 033833 (2002).
[11] D. Petrosyan and Y. P. Malakyan, Phys. Rev. A 70, 023822 (2004).
[12] Z.-B. Wang, K.-P. Marzlin, and B. C. Sanders, Phys. Rev. Lett. 97, 063901 (2006).
[13] M.A.Antón et al., Opt.Commun. 281,6040(2008).
[14] C. Ottaviani, D. Vitali, M. Artoni, F. Cataliotti, and P. Tombesi, Phys. Rev. Lett. **90**, 197902 (2003).

[15] C. Ottaviani et al., Eur. Phys. J. D 40, 281 (2006).

[16] J. D. Pritchard, K. J. Weatherill, C. S. Adams, *Nonlinear optics using cold Rydberg atoms* Annual Review of Cold Atoms and Molecules, 1, **301** (2013)

[17] M. Saffman, T. G. Walker, and K. Mölmer, *Quantum information with Rydberg atoms* Rev. Mod. Phys. **82**, 2313 (2010)

[18] K. Hammerer, A. S. Sorensen, and E. S. Polzik, Rev. Mod. Phys. **82**, 1041-1093 (2010).

[19] A. E. B. Nielsen and K. Molmer, Phys. Rev. A **81**, 043822 (2010).

[20] D. Petrosyan and M. Fleischhauer, Phys. Rev. Lett. **100**, 170501 (2008).

[21] J. D. Pritchard, D. Maxwell, A. Gauguet, K. J. Weatherill, M. P. A. Jones, and C. S. Adams, Phys. Rev. Lett. **105**, 193603 (2010).

[22] T. Peyronel, O. Firstenberg, Q.-Y. Liang, S. Hofferberth, A. V. Gorshkov, T. Pohl, M. D. Lukin, and V. Vuletic, Nature (London) **488**, 57-60 (2012).

[23] O. Firstenberg, T. Peyronel, Q.-Y. Liang, A. V. Gorshkov, M. D. Lukin, and V. Vuletic, Nature (London) **502**, 71-75 (2013).

[24] A. V. Gorshkov, J. Otterbach, M. Fleischhauer, T. Pohl, and M. D. Lukin, Phys. Rev. Lett. **107**, 133602 (2011).

[25] B. He, A. V. Sharypov, J.-T. Sheng, C. Simon, and M. Xiao, Phys. Rev. Lett. **112**, 133606 (2014).

[26] D. Paredes-Barato and C. S. Adams, Phys. Rev. Lett. **112**, 040501 (2014).

[27] M. Khazali, K. Heshami, and C. Simon, Phys. Rev. A **91**, 030301(R) (2015).

[28] D. Yan, C.-L. Cui, Y.-M. Liu, L.-J. Song, and J.-H. Wu, Phys. Rev. A **87**, 023827 (2013).

[29] Y.-M. Liu, X.-D. Tian, D. Yan, Y. Zhang, C.-L. Cui, and J.-H. Wu, Phys. Rev. A **91**, 043802 (2015).

[30] D. Petrosyan, J. Otterbach, and M. Fleischhauer, Phys. Rev. Lett. **107**, 213601 (2011).

[31] I. Friedler, D. Petrosyan, M. Fleischhauer, and G. Kurizki, Phys. Rev. A **72**, 043803 (2005).

[32] A.V. Gorshkov, J. Otterbach, M. Fleischhauer, T. Pohl, and M.D. Lukin, Phys. Rev. Lett. **107**, 133602 (2011).

[33] B. He, A.V. Sharypov, J.-T. Sheng, C. Simon, and M. Xiao, Phys. Rev. Lett. **112**, 133606 (2014).

[34] D. Paredes-Barato and C.S. Adams, Phys. Rev. Lett. **112**, 040501 (2014).

[35] Y.-M. Liu, D. Yan, X.-D. Tian, C.-L. Cui, and J.-H. Wu, Phys. Rev. A **89**, 033839 (2014).

[36] A. Joshi and M. Xiao, Phys. Rev. A **72**, 062319 (2005).

[37] M. D. Lukin, S. F. Yelin, M. Fleischhauer, and M. O. Scully, Phys. Rev. A **60**, 3225 (1999).

[38] C.-L. Cui, J.-K. Jia, J.-W. Gao, Y. Xue, G. Wang, and J.-H. Wu, Phys. Rev. A **76**, 033815 (2007).

[39] This also allows for a vanishing cross Kerr effect such that only Rydberg blockade is responsible for the conditional cooperative nonlinearity shown later.

[40] Each blockade radius can be interpreted as the smallest interatomic distance at which the dipole-dipole interaction moves the Rydberg level out of one EIT window from its center. More details can be found in ref. [30] and ref. [22].

[41] K. Singer, J. Stanojevic, M. Weidemuller, and R. Cote, J. Phys. B: At. Mol. Opt. **38**, S295 (2005).

[42] We find in ref. [22] $N_0 = 2.0 \times 10^{12}$ cm^{-3} and $R_b = 13.0$ μm have been achieved for rubidium atoms in experiment, which then yields $n_{SA} \simeq 18350$.

[43] Both ground collective states $|G\rangle$ and $|M\rangle$ contain $n_{SA}/2$ atoms because each SA contains n_{SA} atoms and these atoms are equally distributed in ground atomic levels $|g\rangle$ and $|m\rangle$.

[44] V. Parigi, E. Bimbard, J. Stanojevic, A. J. Hilliard, F. Nogrette, R. Tualle-Brouri, A. Ourjoumtsev, and P. Grangier, Phys. Rev. Lett. **109**, 233602 (2012).

[45] C. Ates, S. Sevincli, and T. Pohl, Phys. Rev. A **83**, 041802(R) (2011).

[46] A similar averaging has been used in [47] to describe interaction effects in microwave dressed Rydberg atoms and in [44] to explain large dispersive effects in an ensemble of cold Rydberg atoms. Such an approach has also been discussed in [30, 35] and, in particular, in [45] where it has been supported by Monte Carlo simulations.

[47] M. Tanasittikosol, J. D. Pritchard, D. Maxwell, A. Gauguet, K. J. Weatherill, R. M. Potvliege, and C. S. Adams, J. Phys. B: At. Mol. Opt. Phys. 44, 184020 (2011).

[48] A similar behaviour can be observed around point 'β' and hence will not be reported here.